

Tip vortex cavitation suppression and parametric study of an elliptical hydrofoil by water injection

Cite as: Phys. Fluids **35**, 013338 (2023); <https://doi.org/10.1063/5.0130192>

Submitted: 10 October 2022 • Accepted: 02 January 2023 • Accepted Manuscript Online: 03 January 2023 • Published Online: 24 January 2023

 Kang Liu (刘亢),  Ping Wei (魏平),  Liushuai Cao (曹留帅), et al.



View Online



Export Citation



CrossMark

ARTICLES YOU MAY BE INTERESTED IN

[Vortex and cavity dynamics for the tip-leakage cavitation over a hydrofoil](#)

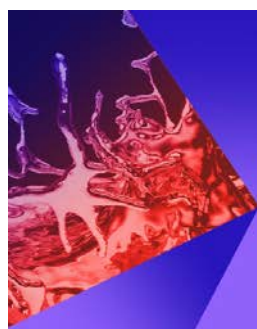
Physics of Fluids **34**, 093303 (2022); <https://doi.org/10.1063/5.0099070>

[Numerical study on cavitation-vortex-noise correlation mechanism and dynamic mode decomposition of a hydrofoil](#)

Physics of Fluids **34**, 125105 (2022); <https://doi.org/10.1063/5.0128169>

[How hydrofoil leading-edge biomimetic structure affects unsteady cavitating flow: A numerical study](#)

Physics of Fluids **35**, 013323 (2023); <https://doi.org/10.1063/5.0131759>



Physics of Fluids

Special Topic: Paint and Coating Physics

Submit Today!

Tip vortex cavitation suppression and parametric study of an elliptical hydrofoil by water injection

Cite as: Phys. Fluids **35**, 013338 (2023); doi: [10.1063/5.0130192](https://doi.org/10.1063/5.0130192)

Submitted: 10 October 2022 · Accepted: 2 January 2023 ·

Published Online: 24 January 2023



View Online



Export Citation



CrossMark

Kang Liu (刘亢),¹  Ping Wei (魏平),²  Liushuai Cao (曹留帅),^{1,a)}  and Decheng Wan (万德成)¹ 

AFFILIATIONS

¹Computational Marine Hydrodynamics Lab (CMHL), School of Naval Architecture, Ocean and Civil Engineering, Shanghai Jiao Tong University, Shanghai 200240, China

²College of Weaponry Engineering, Naval University of Engineering, Wuhan 430033, China

Note: This paper is part of the special topic, Cavitation.

^{a)} Author to whom correspondence should be addressed: liushuaicao@sjtu.edu.cn

ABSTRACT

Tip vortex cavitation (TVC) affects hydrodynamic performance and can cause drastic vibration and noise; therefore, it is crucial to predict the evolution of TVC, understand its generation mechanism, and determine methods to control it. In this work, a large eddy simulation was performed to resolve unsteady turbulence, and the Schnerr–Sauer cavitation model was used to capture transient cavitating flow. Both wetted and cavitating conditions were used in the first step to validate the numerical methods. The mechanism of TVC development and the interactions between the tip vortex and TVC were also revealed. Next, active control by water injection was performed to suppress TVC, and the side and top injection circumstances were explored and compared. Parametric studies were conducted for the side injection condition by changing the injection velocity and angle. The results showed that both side and top injections had remarkable effects on TVC control. Flow field analysis demonstrated that the top injection flow affected the local velocity magnitude and direction of the incident flow of the tip vortex, thus reducing the vortex strength and TVC. For the side injection condition, the injection flow directly influenced the inception structures of the tip vortex. As a result, injection flow deeply deformed the tip vortex and decreased the generation and intensity of TVC. Furthermore, increasing the injection velocity or the component of the velocity in the cross-streamwise direction could effectively increase the cavitation inhibition rate.

Published under an exclusive license by AIP Publishing. <https://doi.org/10.1063/5.0130192>

I. INTRODUCTION

Tip vortex cavitation (TVC) is a common type of cavitation that occurs in offshore equipment and is generated as a result of pressure reduction induced by the swirling movement of a tip vortex.¹ In contrast to sheet and cloud cavitation, which are produced near machine surfaces, TVC is usually generated at the tip region of the propeller or hydrofoil and flows downstream accompanied by the tip vortex. Therefore, TVC has limited influence on the deterioration of the hydrodynamic performance of machines. However, the cyclic process of the formation and collapse of the TVC bubbles will occur along with the development of TVC. During this process, large pressure pulsation will be produced, thereby violently increasing the fluid noise. In addition, when TVC flow develops in the ambient region of the rudder, cavitation bubbles may adhere to its surface, affecting the steering efficiency of the rudder and eroding the rudder surface.² Therefore, it is critical to determine the generation mechanism of TVC and identify methods to inhibit it.

In recent years, scholars have focused on TVC. First, several studies have analyzed the generation of the tip vortex and its cavitation. Batchelor³ determined the mechanism of tip vortex formation, and the results showed that streamwise vortices form to compensate for the discontinuity in velocity circulation. At the same time, the swirling motion caused by the rolling up of the tip vortex dramatically reduced the pressure in the ambient region of the vortex. When the pressure was lower than the saturation pressure under the local temperature, cavitation occurred.⁴ Boulon *et al.*⁵ measured the pressure distribution of the vortex flow on hydrofoils under several flow conditions. In addition, Choi *et al.*⁶ successfully recorded the inception, development, and collapse of cavitation bubbles through high-speed video observations, and the noises in the hydrofoil wake were detected by a hydrophone.

Second, the interactions between the vortex and the cavitation induced by the vortex have also been studied. Hsiao *et al.*⁷ simulated the interactions between two linear vortices with different rotating strengths.

Using the Delft Twist-11 hydrofoil as the object, Ji *et al.*⁸ studied the interactions between cavitation and the vortices of the hydrofoil. The results showed that during the occurrence of TVC, the dilatation term in the vorticity transport process increased significantly. At the same time, through large eddy simulation (LES), Cheng *et al.*⁹ simulated the tip leakage vortex based on the NACA0009 hydraulic hydrofoil and obtained the same results. Xie *et al.*¹⁰ numerically studied the tip vortex flow around an NACA16-020 elliptical hydrofoil and developed a tip vortex model for cavitating flow, which was compared to the wetted flow model. Re_{θ} was used to measure the wall turbulence in a study by Ohta and Sugiura,¹¹ where cavitation was simulated near the wall under Reynolds numbers from 2000 to 2600, to determine the impact of cavitation on the turbulence statistics.

Because cavitation causes severe damage to machinery on ships, controlling cavitation and reducing damage induced by cavitation are extremely important. To achieve these objectives, several scholars have proposed inhibiting cavitation by flow control. This method interferes with the natural flow in the flow field, forcing the redistribution of velocity and pressure in the region through energy input or configuration changes.¹² According to the different modes of control, flow control can be divided into two categories, namely, passive control and active control.

Passive control affects the flow field near the vortex through optimization of the shape or structure of the equipment, by adding wedges, grooving, or subjecting the surface to biomimetic treatment. Kadirav *et al.*¹³ added cavitation-bubble generators (CGs) to the surface of CAV2003 benchmark hydrofoils and studied the effects of CGs with different sizes and locations. To control cavitation, Zhao *et al.*¹⁴ designed a pair of tandem obstacles on the blade suction surface of a waterjet pump as well as conducted unsteady simulations and experiments to study the suppression effects of the tandem obstacles. Based on the experimental analysis, Svennberg *et al.*¹⁵ attempted to delay TVC inception by increasing the roughness of the surface of an elliptical hydrofoil. During analysis, the cavitation number of TVC inception was used for TVC suppression evaluation. The observations indicated that the cavitation number for tip vortex cavitation inception was successfully reduced with the roughness surface with little increase in drag force. Then, in a study by Asnaghi *et al.*,¹⁶ the application of the surface roughness was evaluated on a propeller. The results showed that roughening the blade tip and a limited area of the leading edge resulted in a good TVC mitigation effect with limited hydrodynamic performance degradation. Amini *et al.*¹⁷ investigated the alleviating function of flexible trailing threads to TVC. The researchers found that when the size of a thread was comparable to the viscous core of the tip vortex, the suppression effect would become more pronounced.

Various studies^{13–20} have shown that passive control can be effective in cavitation suppression and does not require additional energy input equipment. However, the disadvantages of this method are that certain shape optimization can suppress cavitation in a specific load range. Therefore, the adaptability of this method under changing load conditions will not be sufficient.

Instead of geometrically optimizing equipment, active control provides mass and energy into the cavitation region and redistributes the velocity and pressure to suppress cavitation. In recent years, many scholars have validated the effectiveness of cavitation suppression using the active control method through experiments and simulations.

Based on experimental studies, several scholars^{21–26} have proposed active flow control for suppressing cavitation. Chahine *et al.*²¹ delayed the TVC of a propeller by using selective polymer injection. According to their results, the viscoelastic properties of the Polyox solution injected in the vortex core played a significant role in thickening the viscous core of the tip vortex, thus reducing the pressure drop in the center region of the tip vortex. Wang *et al.*²² proposed four jet flow types on an NACA66 (MOD) hydrofoil and studied the effects of these methods on cavitation evolution. The results proved that active water injection could effectively suppress sheet and cloud cavitation, and the suppression effects were influenced by the jet rates and jet flow position. Timoshevskiy *et al.*²³ studied the effect of tangential injection on the suction surface of a 2D hydrofoil and use proportional, integral, and velocity filter methods and several hydroacoustic measurements to measure the velocity distribution and identify the cavitating flow. The results showed that tangential injection could effectively reduce the area of cloud cavitation and achieve effective suppression for cavitation. In addition, the injection method could also change the amplitude of pressure pulsations under unsteady regimes. Park *et al.*²⁴ studied TVC suppression in a marine propeller using the cavitation tunnel at Seoul National University (SNU). The researchers proposed a semiactive control method at the propeller tip, and the results showed that this method could effectively suppress TVC generation under the utilized design conditions. Lu *et al.*²⁵ arranged a row of injection holes on the suction surface of the NACA0066 hydrofoil, and the cavitation structures under unsteady cavitation conditions and water injection conditions were visualized using the high-speed flow field display technology. Lee *et al.*²⁶ applied water injection to control TVC and achieved noise suppression using an NACA0020 elliptical hydrofoil and a five-blade propeller. According to the results, the water injection method could effectively delay TVC inception and reduce the noise induced by TVC.

Computational fluid dynamics has also shown to be a productive tool in cavitation suppression. Zhao *et al.*²⁷ proposed active flow in a centrifugal pump to control cavitation, where the modified $k - \omega$ shear stress transport model combined with the Kubota cavitation model was used for simulation. On an NACA0015 hydrofoil, De Giorgi *et al.*²⁸ performed active control by a single synthetic jet actuator (SJA), using the Eulerian homogeneous mixture/mass transfer model and Schnerr–Sauer cavitation model in the simulations. Furthermore, the researchers used proper orthogonal decomposition to highlight the benefit of the SJA for suppressing the thickness growth of the sheet cavity. By employing the $k - \varepsilon$ renormalization group turbulence model and full cavitation model, Wang *et al.*²⁹ investigated the impact of jet hole locations and porosities along a 3D NACA66 (MOD) spanwise hydrofoil on cavitation suppression. The researchers³⁰ also used the double-row jet hole scheme and clarified the influence of water injection on the broadband noise and hydrodynamic performance using the density-corrected turbulence model combined with the Zwart–Gerber–Belamri cavitation model. The results showed that water injection was effective for drag reduction and noise suppression. Pant *et al.*³¹ numerically studied the effect of active control on unsteady cavitation. The researchers selected OpenFOAM as the simulation platform and used the LES turbulence model and Sauer–Schnerr cavitation model during numerical calculations. The interaction of the re-entrant jet with the wall jet was analyzed, and the analysis revealed that this interaction could cause a large transformation in pressure distribution, thus counteracting the local increase in pressure.

As verified by existing research, the water injection method can effectively control cavitation in hydrofoils and propellers. Moreover, water injection can also effectively suppress the operating noise induced by cavitation bubbles. However, at present, only a few studies have conducted simulations of active injection on the tip vortex and its cavitation and analyzed its suppression effects on TVC as well as sub-sequent interactions among the water jet, tip vortex, and TVC. Therefore, in this study, we examined the interactions between injecting flow and tip vortex flow to understand the water injection method mechanism in suppressing TVC.

STAR-CCM+ software was used to simulate the TVC phenomenon in an elliptical hydrofoil with the NACA0012 cross section, and the LES turbulence model and Schnerr–Sauer cavitation model were selected for the simulations. The remainder of the manuscript is organized as follows. Section II describes the numerical methods used in STAR-CCM+, while the geometric model, meshing method, and boundary conditions are described in Sec. III. Validation of the numerical methods performed by wetted and cavitating simulations is explained in Sec. IV, Sec. V describes the results and analyses under different water injection conditions, and Sec. VI presents the conclusions.

II. METHODOLOGY

Navier–Stokes (N–S) equations are always used in hydrodynamics studies to mathematically describe the conservation of momentum and mass during flowing. For different engineering purposes, the N–S equations have been simplified to yield several numerical turbulence models, namely, Reynolds-Average Navier–Stokes (RANS), Scale resolving simulation (SRS), and direct numerical simulation (DNS).³² In simulation, the RANS method can only obtain acceptable results with fewer computational resources, whereas DNS requires more computational resources. The LES model is the widely used turbulence model for TVC simulations among SRS, and several scholars have performed numerical studies involving complex field problems using the LES method and acquired satisfactory results.^{33–38}

A. Governing equations

By directly resolving most of the turbulence information in the flow domain and modeling small-scale information, the LES method can obtain more accurate results than the RANS method and will consume fewer resources than DNS. The governing equations under the LES framework are shown below:³⁹

$$\frac{\partial \rho}{\partial t} + \frac{\partial \rho \bar{u}_i}{\partial x_i} = 0, \tag{1}$$

$$\frac{\partial \rho \bar{u}_i}{\partial t} + \frac{\partial \rho \bar{u}_i \bar{u}_j}{\partial x_j} = -\frac{1}{\rho} \frac{\partial \bar{p}}{\partial x_i} + \frac{\partial}{\partial x_j} \left(\mu \frac{\partial \bar{u}_i}{\partial x_j} \right) - \frac{\partial \tau_{ij}}{\partial x_j}, \tag{2}$$

where ρ is the density of the fluid, \bar{u}_k ($k = i, j$) is the velocity after filtering, \bar{p} is the pressure after filtering, τ_{ij} denotes the stresses, μ_t is the turbulent viscosity coefficient, and μ is the viscosity coefficient under single-phase homogenization.

B. Subgrid-scale (SGS) modeling

In the wall-adapting local-eddy viscosity (WALE) LES method used in this study, τ_{ij} was calculated by the following equation:⁴⁰

$$\tau_{ij} = \bar{\tau} + \bar{\tau}_{SGS} = \rho (\bar{u}_i \bar{u}_j - \bar{u}_i \bar{u}_j), \tag{3}$$

where $\bar{\tau}$ is the stress after filtering and $\bar{\tau}_{SGS}$ is the SGS stress. Based on the Boussinesq hypothesis, the SGS stress could be modeled by

$$\bar{\tau}_{SGS} = 2\mu_t S_{ij} - \frac{2}{3} \left(\mu_t \frac{\partial \bar{u}_i}{\partial x_i} \delta_{ij} \right), \tag{4}$$

where S_{ij} denotes the strain rate tensor, δ_{ij} is the identity tensor, and μ_t is the SGS turbulence viscosity and should be redescribed in SGS models. In the WALE subgrid model, S_{ij} and μ_t can be computed using the following equations:

$$S_{ij} = \frac{1}{2} \left(\frac{\partial \bar{u}_i}{\partial x_j} + \frac{\partial \bar{u}_j}{\partial x_i} \right), \tag{5}$$

$$\mu_t = \rho \Delta^2 S_w, \tag{6}$$

where Δ is the length scale to determine the width of the small vortex and S_w is the deformation parameter. The details of the resolved equations can be found in the STAR-CCM + User Guide (2020).⁴⁰

C. Cavitation model

The volume of fluid (VOF) model is a simple multiphase model and the foundation of cavitation modeling. During cavitation, it can be used to describe the water and vapor phases, and detailed information regarding the VOF model is clearly presented in the STAR-CCM + User Guide (2020).⁴⁰

In STAR-CCM+, three models can be selected to simulate cavitation: the Full Rayleigh–Plesset model, the Homogeneous Relaxation model, and the Schnerr–Sauer model. The Schnerr–Sauer cavitation model used in this study was based on the Rayleigh–Plesset equation and neglected the influence of bubble growth acceleration, viscous effects, and surface tension effects. Its effectiveness on tip vortex cavitation prediction has been well proven in the previous studies.^{41–44} Furthermore, this model has been widely implemented in commercial software. Therefore, the Schnerr–Sauer cavitation model was selected for computation.

During cavitation and gas dissolution, STAR-CCM+ made two assumptions. First, the seeds were considered spherical and uniformly distributed in the liquid so that they can be described by the number of seeds per unit volume of liquid n_0 . Second, all seeds had the same radius at the beginning of cavitation.

With the above assumptions, the relationships between the number of seeds N and a control volume V could be expressed by the following equation:

$$N = n_0 \alpha_l V, \tag{7}$$

where α_l is the volume fraction of liquid in V .

The total volume of vapor V_v follows:

$$V_v = NV_b, \tag{8}$$

where V_b is the volume of one bubble and can be calculated by the local bubble radius R ,

$$V_b = \frac{4}{3} \pi R^3. \tag{9}$$

With Eqs. (7)–(9), the volume fraction of vapor a_v can be expressed by

$$a_v = \frac{V_v}{V} = \frac{NV_b}{V} = \frac{4}{3} \pi R^3 n_0 \alpha_l. \tag{10}$$

When bubbles moved with the flow, the volume change of every individual bubble could be represented by the following equation, where v_r denoted the bubble growth velocity,

$$\frac{dV_b}{dt} = 4\pi R^2 v_r. \quad (11)$$

To describe the growth and collapse of vapor in cavitation, the volume change of vapor in the control volume could be represented by a source term

$$Q_V = N \frac{dV_b}{dt} = 4\pi n_0 (1 - \alpha_r) V R^2 v_r. \quad (12)$$

If vapor was present in the form of bubbles, whose radius was the same, the relationship between the vapor and liquid phases was as follows:

$$V_v = \frac{4}{3} \pi n_0 V_l R^3. \quad (13)$$

Therefore, the volume fraction of vapor could be redescribed in the following equation, and the bubble radius and seed diameter could be calculated by α_v ,

$$\alpha_v = \frac{V_v}{V} = \frac{V_v}{V_v + V_l} = \frac{\frac{4}{3} \pi n_0 R^3}{1 + \frac{4}{3} \pi n_0 R^3}. \quad (14)$$

In the Schnerr–Sauer cavitation model, the growth rate of bubble radius was estimated by the following model:⁴⁵

$$v_r = \frac{2}{3} \left(\frac{p_v - p}{\rho_l} \right). \quad (15)$$

III. SOLVER SETUP

A. Geometric model and simulation setup

An elliptical hydrofoil with the NACA0012 cross section was selected for this study, as the hydrodynamic performance and cavitation structures were obtained from the experiments of Takasugi *et al.*⁴⁶ Its maximum chord and span length were 150 and 176.7 mm, respectively. The geometric model of the hydrofoil is shown in Fig. 1(a), in which C denotes the maximum chord length of the hydrofoil and S denotes the maximum span length.

The domain for the simulation was set as shown in Fig. 1(b). The maximum chord length C was set as the scale of measurement for the length, width, and height of the computational domain, which were $16C$, $3C$, and $3C$, respectively. The flow direction denoted the x direction of the domain, and the normal and spanwise directions of the hydrofoil, respectively, denoted the y and z directions. As shown in Fig. 1(b), the elliptical hydrofoil was located at the center of the domain along the x and y directions to reduce the influences of the inlet, outlet, and walls on the results. However, in the z direction, the hydrofoil could only be placed at the bottom, considering the actual installation conditions during the experiments.

B. Mesh generation

During the rolling up and transportation processes of the vortex, the structures of the tip vortex and its cavitation had very small scales, and the flow in the ambient region of the tip vortex changed drastically. Even a minute numerical deviation during calculations could yield incorrect results; therefore, a smaller cell scale was needed near the tip vortex region. In addition, because the structure of the tip vortex was not a perfect slender cylinder but was curved toward the bottom of the domain, it was difficult to refine the tip vortex region by the structured meshing method. Considering the reasons mentioned above, automated trimmer meshing and volumetric refinement were used (Fig. 2).

In the mesh settings, the basic size of the domain was set as S_b ; the maximum cell size was set as $32 S_b$, and a smaller cell size ($2 S_b$) was used on the hydrofoil surface. At the same time, to ensure that the mesh structure did not change when the working conditions changed, some of the surfaces near the tip of the hydrofoil were isolated from the hydrofoil surface and set as the surfaces of the injection holes (red: top injection, blue: side injection) so that water injection could be realized merely by adjusting the boundary conditions at the surfaces of the injection holes. Moreover, the cell size of the injection holes was set to $0.2 S_b$.

To obtain better TVC calculation results, the domain near the hydrofoil and TVC need to be refined. First, one $5C \times 2C \times 2C$ ($x \times y \times z$) block region, known as the buffer region, was refined around the hydrofoil, and one cylinder with 35-mm radius was meshed at the tip region to obtain an acceptable flow trend around the elliptical hydrofoil. The cell sizes in the buffer block and cylinder were $8 S_b$ and $2 S_b$, respectively. Then, the simulation was carried out based

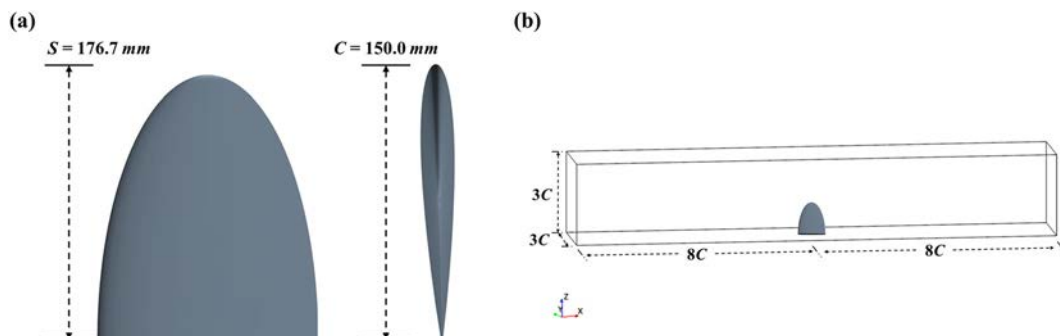


FIG. 1. Geometric model of NACA0012 elliptical hydrofoil and numerical domain: (a) geometric model and (b) numerical domain.

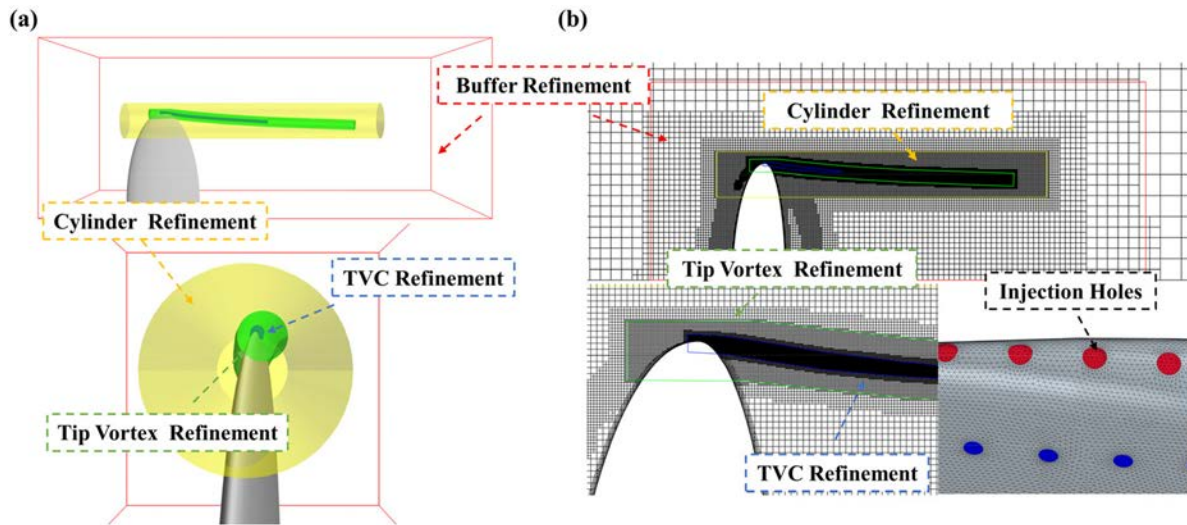


FIG. 2. (a) Location of the refinement regions and (b) the final mesh.

on initial meshing so that the structure of the tip vortex could be identified by the iso-surface with a Q -criterion = $10\,000\text{ s}^{-2}$. Second, based on the view of the Q -criterion iso-surface, one irregular geometry with a cell size of $0.5 S_b$ was built for tip vortex refinement. After obtaining the results based on the meshing of tip vortex refinement, the value of the Q -criterion iso-surface was increased to $100,000\text{ s}^{-2}$ to capture the region where TVC could occur, as TVC occurred in the core region of the tip vortex. Finally, similar to the process mentioned above, an irregular geometry was built for TVC refinement with a cell size of $0.125 S_b$.

C. Initial and boundary conditions

In the following simulation, the boundary of the domain inlet was set as the velocity inlet and the velocity at the inlet was $V_I = 6\text{ m/s}$. The outlet was the pressure outlet, and the pressure values were 0 and

$39\,278\text{ Pa}$ under open water and cavitation conditions, respectively. The surfaces on the domain side and hydrofoil were set as the walls. During numerical calculations, second-order time discretization was used; the time step was $5 \times 10^{-5}\text{ s}$, and 20 iterations were conducted in each time step; the lift coefficient, continuity, and momentum in the x , y , and z directions of the hydrofoil were monitored to identify the convergence of the solution.

IV. NUMERICAL PROCEDURES

A. Numerical validation

To determine whether the mesh resolution met the accuracy requirements of cavitation prediction, the simulations under four different mesh configurations, namely, coarse (basic size was 0.002 m), medium (basic size was 0.0014 m), fine (basic size was 0.001 m), and very fine (basic size was 0.0007 m), were performed. Figure 3(a) shows the cross section views and layout details of the different meshes, and

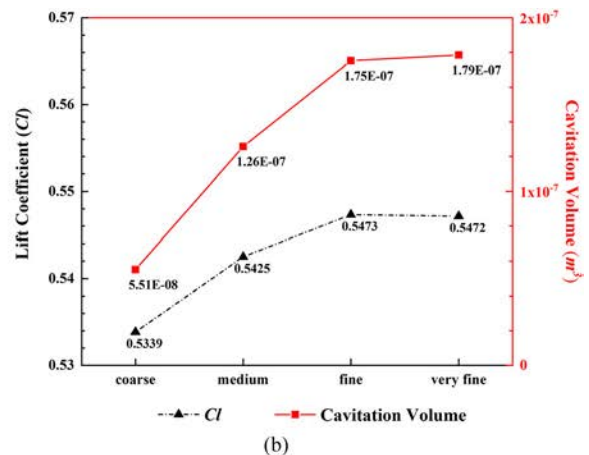
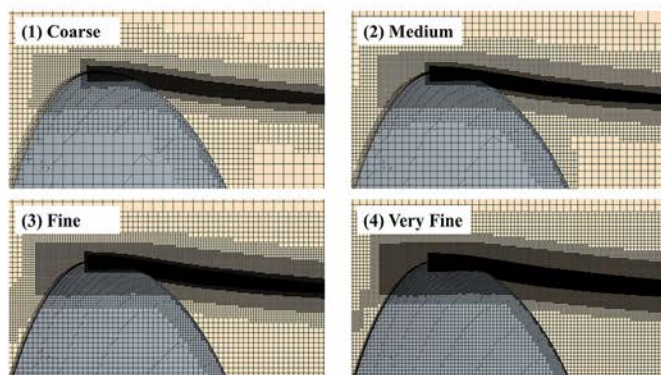


FIG. 3. Mesh independence study: (a) cross section views of the four mesh layouts and (b) lift coefficient and cavitation volume curves vs the four mesh cases.

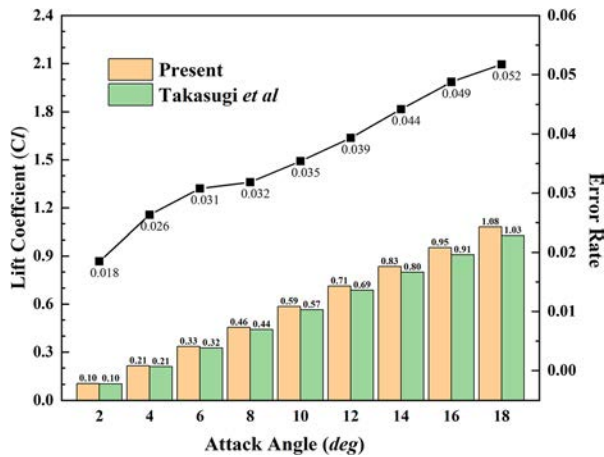


FIG. 4. Comparison of the lift coefficient obtained in the present simulation and in the experiment by Takasugi *et al.*⁴²

Fig. 3(b) presents the results of the lift coefficient and cavitation volume curves, respectively. This proved that both the lift coefficient and cavitation volume converged as the basic size of the domain increased. Moreover, according to the research reported by Ahmad *et al.*,⁴⁷ 30–40 grid points across the core region of a vortex were recommended for the second-order accurate solver. In the TVC simulation of Asnaghi *et al.*,⁴⁸ 32 grid points were used across the vortex core. In this study, when a fine mesh level was achieved, about 30 grid points were placed in the crosswise direction in the vortex core region, which correlated with the criteria mentioned above. Considering the balance of computational cost and solution accuracy, the fine mesh was finally selected to carry out the following simulations.

In the next step, we simulated flow around the hydrofoil in open water, wetted, and cavitating conditions and compared the results with

TABLE I. Comparison of the lift coefficients obtained in the cavitation condition.

	Lift coefficient		Error	Error rate
	Present	Takasugi <i>et al.</i> ⁴²		
10	0.585	0.565	0.020	3.5%

those obtained experimentally by Takasugi *et al.*⁴² To verify the correctness of the simulation, the hydrodynamic coefficient (lift coefficient C_l) of the hydrofoil was calculated under open water conditions and compared to the results obtained experimentally by Takasugi *et al.*,⁴² as shown in Fig. 4.

Figure 4 shows that the lift coefficient determined in the present simulation agreed with the values determined by Takasugi *et al.*⁴² Although the error between the present simulation and experiment increased with increasing attack angle, the maximum error rate was approximately 5.2%. Furthermore, the error rate given in Table I for $\alpha = 10^\circ$, which was used in the following cavitation simulation, was approximately 3.5%.

Second, based on the tip vortex simulation, the Schnerr–Sauer cavitation model was added in the simulation, where the wetted and cavitating conditions were selected to explore the mechanism of TVC generation as well as the interactions between the tip vortex and its cavitation. In the simulation, $V_I = 6$ m/s, the attack angle was $\alpha = 10^\circ$, and the cavitation numbers were $\alpha_n = 2.01$ and 1.3, as shown in Figs. 5 and 6, respectively. Table II presents the settings used for the simulation.

Figures 5 and 6 compare the numerical and experimental results. The TVC development trend in the experiment by Takasugi *et al.*⁴² and the present simulation were shown in Fig. 5. The inception position and structure of the TVC in the simulation showed great agreement with the results of Takasugi *et al.*⁴² However, a thin small layer of sheet cavitation was captured on the leading edge of the hydrofoil in the present study, which was not clearly visible in the experiments. The velocity profile on the 90% span position was compared in Fig. 6. Despite the slight deviation, the flow trend corresponded well with the experiment. It demonstrated that based on the numerical methods adopted in the paper, the tip vortex flow field could be successfully simulated.

To identify the influence of TVC on tip vortex flow, the flow trends and pressure distributions around the tip vortex were analyzed using streamlines and pressure contours based on the simulation results. Subsequently, the differences between the tip vortices in the wetted and cavitating conditions were compared.

The flows near the TVC region were visualized using the streamlines in the left column of Fig. 7. In the next step, the instantaneous pressure distributions and velocity streamlines were obtained at $x = 0.1$ (the position of TVC inception), as illustrated in the right column of Fig. 7.

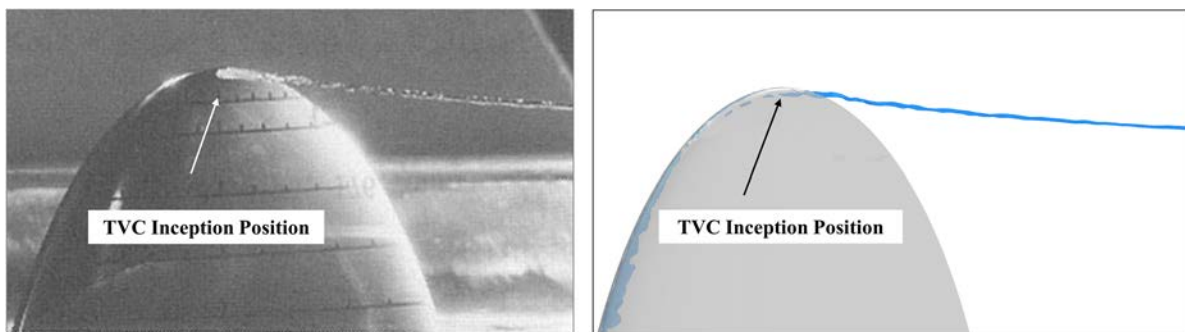


FIG. 5. Comparison of the results obtained under cavitating conditions in the present simulation (right) and those obtained by Takasugi *et al.*⁴² (left).

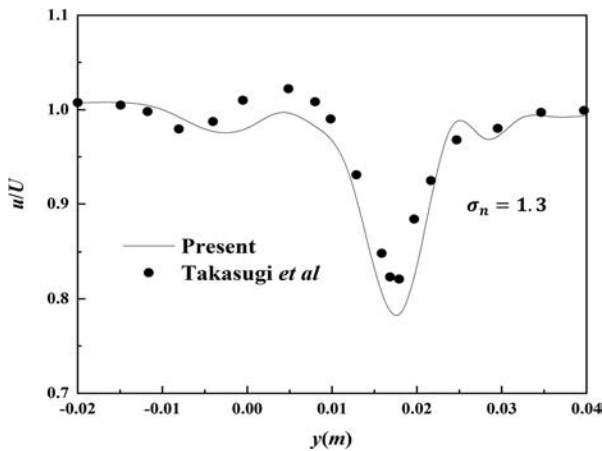


FIG. 6. Velocity profile comparison in the 90% span position.

TABLE II. Model settings for NACA0012.

Variables	Symbols	Case setting
Inlet velocity	V_I	6.0
Attack angle	α	10
Saturation pressure	p_v	3170.34
Density of water	ρ_w	997.561
Density of vapor	ρ_v	0.595 31
Dynamic viscosity of water	μ_w	8.8871×10^{-4}
Dynamic viscosity of vapor	μ_v	$1.267 65 \times 10^{-5}$

First, the streamlines shown in the left column of Fig. 7 demonstrated that the flow trend under the wetted condition was similar to that of the cavitating condition. The generation of TVC had only a slight impact on the local flow around it. However, as shown in the pressure distribution at $x = 0.1$, the pressure distribution details under the wetted and cavitating conditions were quite different. Under the wetted condition, the strong swirl of the tip vortex led to a pressure reduction in the vortex core region, generating a low-pressure region, which subsequently caused the generation of TVC. After cavitation occurred, the cavitation bubbles compensated for the low-pressure region and reduced the pressure gradient induced by swirling motion.

Second, the swirling streamlines in the pressure distribution diagram showed that the rotation trends of the tip vortex were roughly the same under these two conditions. In the inception position of the tip vortex, the fluid from the pressure side of the hydrofoil tended to move upward. After crossing the tip region, the flow direction gradually became bent and turned to the suction side (indicated by the yellow arrow in Fig. 7). Then, the flow converged near the suction side surface and formed the rejection flow (indicated by the black arrow in Fig. 7). Hence, the rotating movement of the tip vortex flow could be divided into two parts, namely, the incident flow from the pressure side and the rejection flow to the suction side.

Furthermore, Fig. 8 depicts the influence of TVC on the tip vortex structures, indicating the iso-surface with the Q-criterion of the tip vortex. In addition, to clarify the influence of TVC on the tip vortex, the tip vortex structure at $x = 0.1$ was enlarged.

Figure 8 shows that the development of the tip vortex under the two conditions was not significantly different. In the wetted and cavitating conditions, the tip vortices were curved downward and presented bow-like shapes. Specifically, as TVC was generated at the core

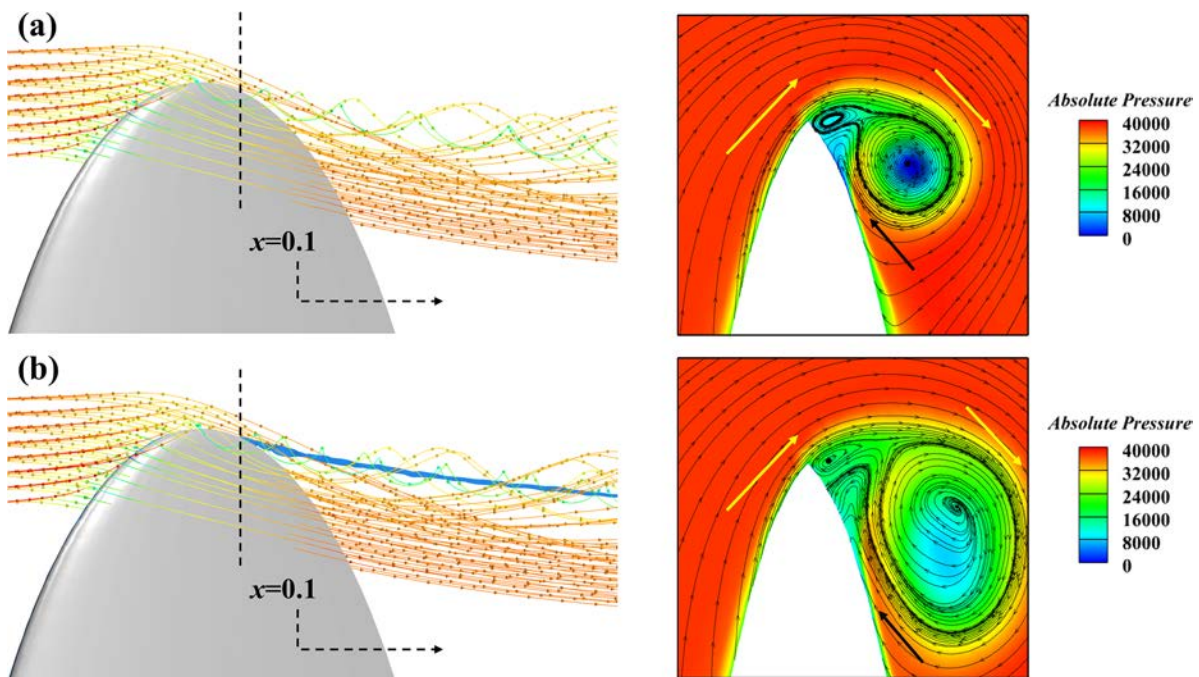


FIG. 7. Flow streamlines around the NACA0012 hydrofoil: (a) wetted condition and (b) cavitating condition.

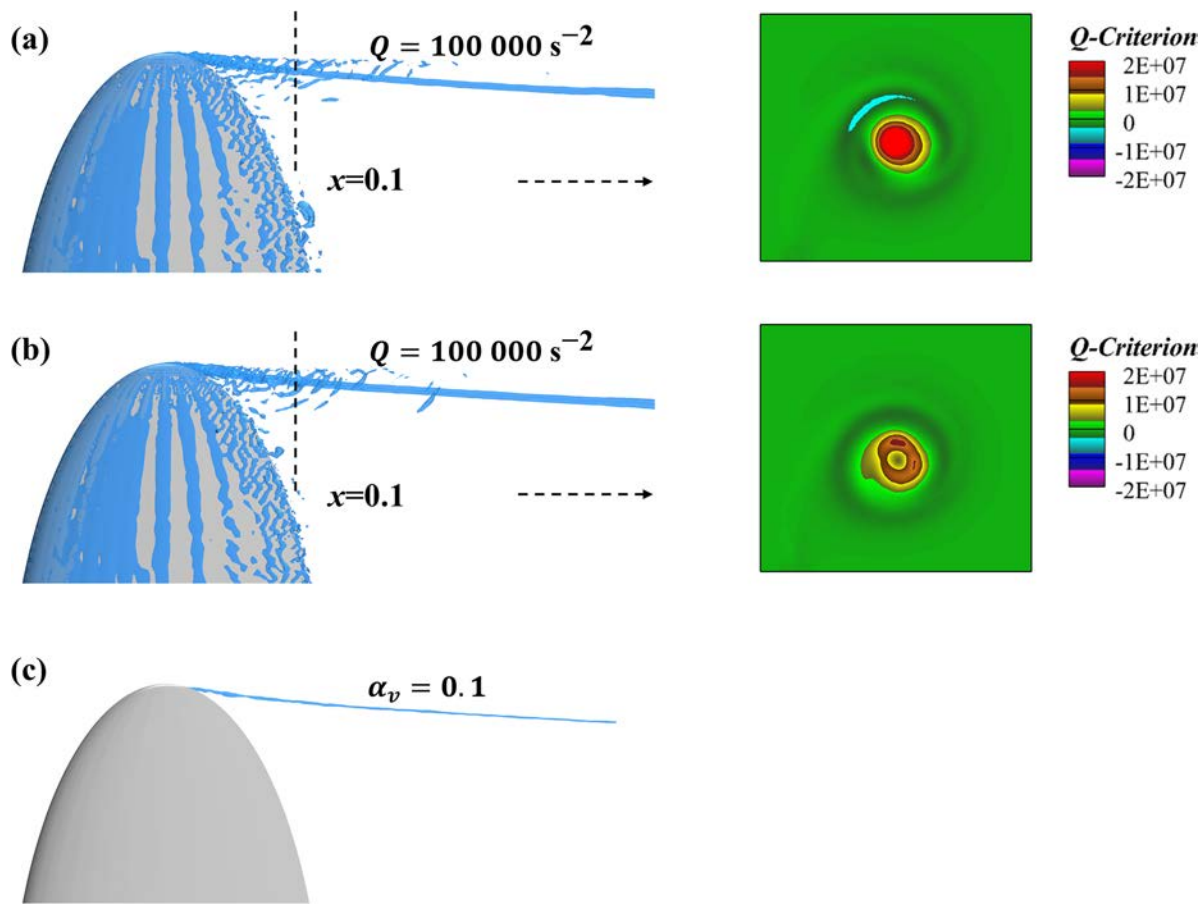


FIG. 8. Tip vortex and TVC structure in wetted and cavitating conditions: (a) $Q = 100\,000\text{ s}^{-2}$ in wetted condition, (b) $Q = 100\,000\text{ s}^{-2}$ in cavitating condition, and (c) $\alpha_v = 0.1$ in cavitating condition.

region of the tip vortex, TVC also presented the same shape as the tip vortex.

However, as shown in the right column of Fig. 8, the Q -Criterion distribution of the tip vortex at $x = 0.1$ revealed differences in the shape of the vortex core under the two working conditions. Under the wetted condition, the strength inside the vortex core was extremely strong, as indicated by the pure red color. Under the cavitating condition, the strength of the vortex core was significantly reduced. In addition, the shape of the tip vortex changed considerably in the cavitating condition. Under the wetted condition, the shape of the tip vortex was solid and expanded almost equally in the radial direction. However, after TVC occurred, as the vortex strength in the region where TVC was generated decreased dramatically, the shape of the vortex became annular.

V. RESULTS AND DISCUSSION

After verifying the accuracy of the selected models, obtaining the flow trend of the tip vortex, and determining the generation reasons for TVC, the active injection method was included in the simulation for TVC suppression. First, two water injection locations were selected to validate the suppression effect of the water injection method on

TVC. Then, from 0 to 12 m/s, the injection velocities were separated into five grades and the influence of the injection velocities on the tip vortex and its cavitation was analyzed, as discussed in Sec. V B. Finally, the influences of the injection angles were explained, as presented in Sec. V C.

A. TVC control by side and top water injection

As shown in Fig. 9, seven injection holes with a diameter of 1 mm were opened in the tip area in this section. According to the different positions of the injection holes, the water injection method could be divided into two types, namely, side injection and top injection, and the effect of active injection on cavitation suppression was studied using these two methods. Along the normal direction of the holes, water was injected into the cavitation region with an injection speed of $V_j = 1.5 V_I$.

As shown in Fig. 9(a), the opening positions of the holes were located at the suction side and 2 mm from the center along the trailing edge. The positions were close to the inception area of TVC, and the injected water could directly influence the development of the tip vortex. As shown in Fig. 9(b), injection holes opened along the centerline of the trailing edge. The positions were far away from the tip vortex

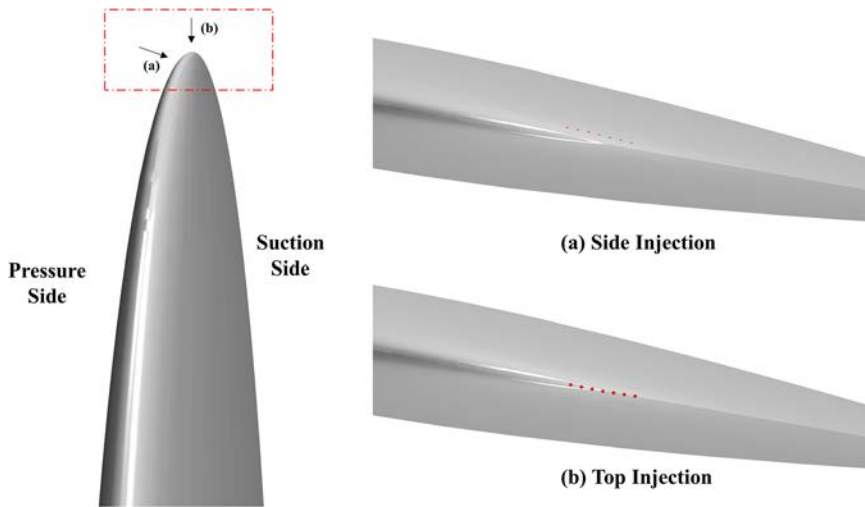


FIG. 9. Positions of the injection holes: (a) side injection and (b) top injection.

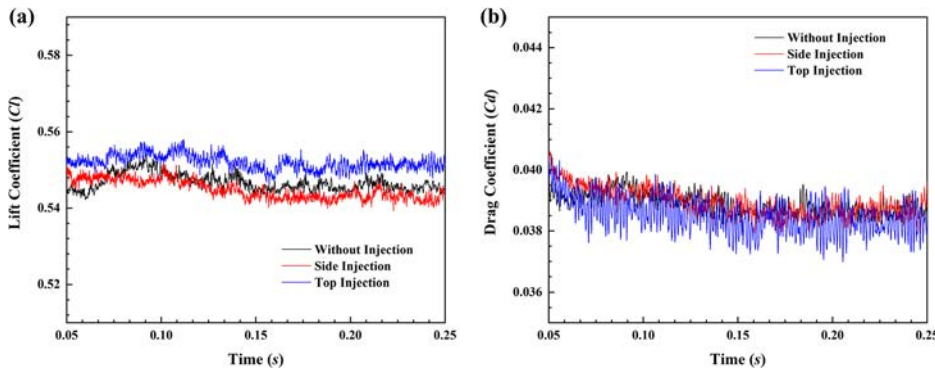


FIG. 10. Force coefficient comparison under W/O, S/I, and T/I conditions.

region, and the injection flow could only affect the tip vortex through the movement of the flow field.

As a thrust machine, the most important characteristic of an elliptical hydrofoil is its hydrodynamic performance, such as lift and drag performance. In this study, the lift coefficient C_l and drag coefficient C_d of the elliptical hydrofoil were measured under three working conditions, namely, without injection (W/O), top injection (T/I), and side injection (S/I). Figure 10 shows the change curves of C_l and C_d over time under the three working conditions, and the time-averaged coefficients were recorded, as shown in Table III. To ensure that the flow was stabilized during time-averaged calculation, only the results in the period after $t = 0.2$ s were involved. Furthermore, a higher lift-to-drag ratio indicated higher propulsion performance with less resistance, and this could improve the efficiency of ship appendages.^{49–51}

TABLE III. Comparison of the force coefficients under W/O, S/I, and T/I (C_l : lift coefficient and C_d : drag coefficient).

Condition	C_l	C_d	K
W/O	0.547	0.0388	14.39
S/I	0.545	0.0387	13.90
T/I	0.553	0.0388	14.55

The lift-to-drag ratios under the three working conditions were compared, as presented in Table III. The lift coefficient C_l , drag coefficient C_d , and lift-to-drag ratio K could be defined as follows:

$$C_l = \frac{F_l}{0.5\rho U^2 S_l}, \tag{16}$$

$$C_d = \frac{F_d}{0.5\rho U^2 S_d}, \quad \text{and} \tag{17}$$

$$K = \frac{C_l}{C_d}, \tag{18}$$

where F_l and F_d are the lift and drag, respectively, and S_l and S_d denote the projection areas of the elliptical hydrofoil in the y and z directions, respectively.

As shown in Fig. 10, the distributions of C_l and C_d along with the varying physical times were nearly the same under the three conditions. Only the pulsation frequency of C_d in the top injection condition was higher than it under S/I and W/O. The results in Table III showed that the drag coefficients under the three conditions were roughly the same. The lift coefficient and lift-to-drag ratio under the top injection condition were both higher and about 1.1% than the condition without injection, while they were lower by about 0.36% and 3.4%, respectively, under the side injection condition.



FIG. 11. TVC structures in the three conditions: (a) W/O, (b) S/I, and (c) T/I.

To compare the TVC suppression effects of the two injection methods, the cavitation structures in the three conditions were visualized based on the iso-surface of the volume fraction of the vapor α_v , as shown in Fig. 11. The cavity volumes of the cavitation bubbles in the three conditions are listed in Table IV.

First, in the cavitating condition, TVC developed a long distance toward downstream and could be clearly captured, and the cavity volume captured by the simulation in this condition was $2.38 \times 10^{-7} \text{ m}^3$. Second, in the S/I condition, the volume of the cavitation bubbles was $0.61 \times 10^{-7} \text{ m}^3$. Compared to the cavitating condition, the volume of vapor decreased by about $1.17 \times 10^{-7} \text{ m}^3$, and TVC produced by the hydrofoil almost disappeared. Finally, according to Table IV, T/I could inhibit the inception of TVC by about $0.68 \times 10^{-7} \text{ m}^3$. The results indicated that both injecting water in the side and top regions could

effectively mitigate the generation of TVC, and side injection had a better effect. At the same time, some cavitation bubbles were generated behind the injection hole positions in both injection methods, as the injection flow changed the direction of the flow near the holes.

According to the flow field analysis in Fig. 7, the TVC of the hydrofoil was derived from the pressure reduction produced by the rotation effect of the tip vortex. Therefore, exploring the effect of injection on tip vortex motion was an effective way to determine the influence of injection on cavitation inhibition. In this study, the slides at the center of the injection holes were extracted, and the Q -criterion contours and local streamlines were used to visualize the flow trend of the tip vortex. Subsequently, the influences of injection flow on the tip vortex structure were analyzed based on the results.

The tip vortex core was clearly indicated by the red region in Fig. 12(a), and the region bounded by the tip vortex core was the TVC position. In the W/O condition, the structures of the tip vortex and its cavitation were stable. The TVC was wrapped by the tip vortex core region, as shown in Fig. 12(a), and Fig. 12(a) also shows the inception and mature positions of the tip vortex. When $x = 0.073$, the tip vortex was still in the nascent stage, where it was very small and close to the surface of the hydrofoil. When the vortex developed to the position where $x = 0.082$, it was completely detached from the surface of the hydrofoil and fully formed.

The disturbance effect of the two injection methods on the tip vortex could be determined from Fig. 12.

TABLE IV. Comparison of the cavity volumes of the hydrofoil under different injection conditions.

Condition	Cavity volume ($\times 10^{-7} \text{ m}^3$)	Injection speed (m/s)	Change rate of the cavity volume
W/O	1.75	9	...
S/I	0.58	9	0.67
T/I	1.07	9	0.39

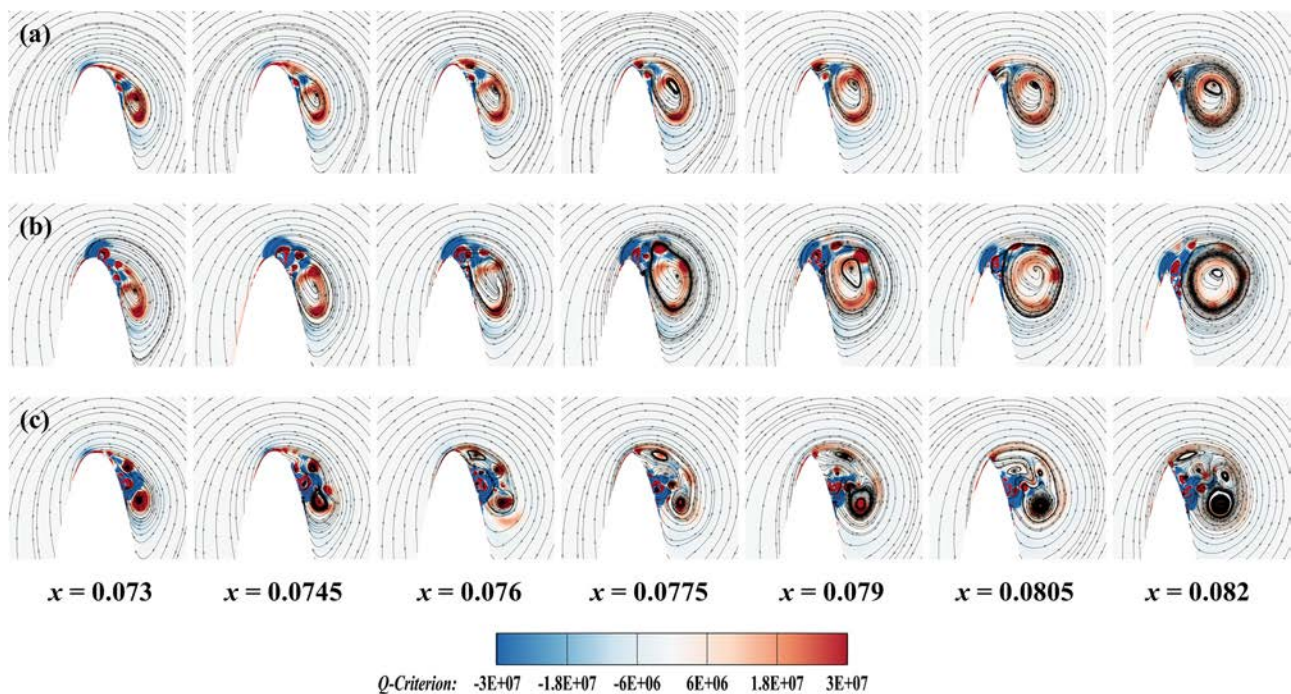


FIG. 12. Comparison of the tip vortex structures during the vortex development: (a) W/O, (b) T/I, and (c) S/I.

According to Figs. 12(b) and 12(c), the energy carried by the injection flow would significantly damage the vortex structure near the injection region when the holes were opened vertically or laterally. The degree of damage differed between the two injection methods due to the different locations of the holes.

Under the T/I condition shown in Fig. 12(b), the injection flow only destroyed the vortex formed at the tip position, and the structure of the tip vortex was relatively intact. Although there was a slight increase in the diameter of the tip vortex under the T/I condition compared to the W/O condition, their development trends were similar.

However, the tip vortex structure changed drastically under the S/I condition, as opposed to the T/I condition. As shown in Fig. 12(c), because the flow injected by the lateral holes could directly act on the core region of the tip vortex and its cavitation, the tip vortex was decomposed into several disordered and smaller vortices. Under this action, the disorderliness of the flow in the vortex core area increased and the directional rotation intensity of the tip vortex decreased. Subsequently, the pressure drop caused by the rotation also showed a decreasing trend, and the generation of TVC was inhibited.

Directly destroying the tip vortex structures was shown to effectively inhibit the development of TVC, and this was one reason S/I had such a significant effect on the suppression of TVC. In addition to directly destroying the tip vortex, forcing the flow trends of the tip vortex could also affect TVC generation. As mentioned above, under the T/I condition, only the vortex formed at the tip position was destroyed and the tip vortex still was intact. The reason why top injection could

also effectively suppress TVC was it influenced the flow trends. To analyze the flow field around the opening positions more clearly, the flow field at the typical position ($x = 0.073$) was enlarged, as shown in Fig. 13.

As mentioned in Sec. IV, the rotational motion of the tip vortex could be divided into two parts. One part was the incident flow from the pressure side of the elliptical hydrofoil, and the other one was the rejection flow to the suction side surface. Compared to the flow trend shown in Fig. 13(a), the trend shown in Fig. 13(b) indicated that the vertical fluid jet could effectively change the direction and velocity of the incident flow, subsequently reducing the rotation intensity of the hydrofoil tip vortex, and reduce the vortex core pressure drop. Based on the same principle, as shown in Fig. 13(c), S/I had an impact on the rejection flow of the tip vortex. However, because this method also caused severe damage to the tip vortex structure, the effect of rejection flow redistribution caused by S/I on the suppression of the tip vortex rotation intensity could not be effectively analyzed. In summary, T/I only inhibited TVC generation by redistributing the tip vortex flow, and S/I could influence TVC by directly damaging the structure of the tip vortex and redistributing the flow.

B. Injection velocity control in water injection methods

After verifying the effect of water injection on TVC suppression, the injection velocity and angle were selected to analyze the parametric

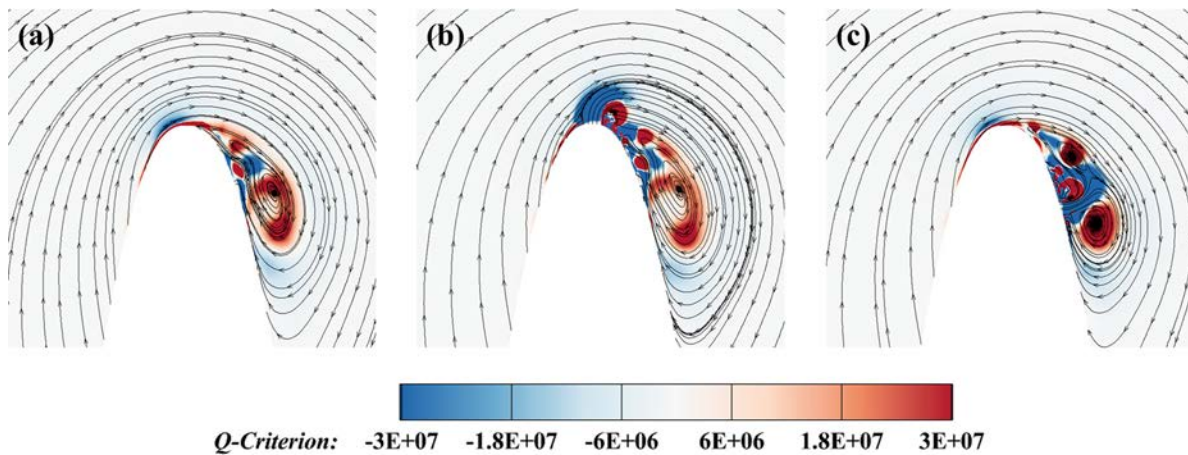


FIG. 13. Comparison of the tip vortex structures in the vortex inception position: (a) W/O, (b) T/I, and (c) S/I.

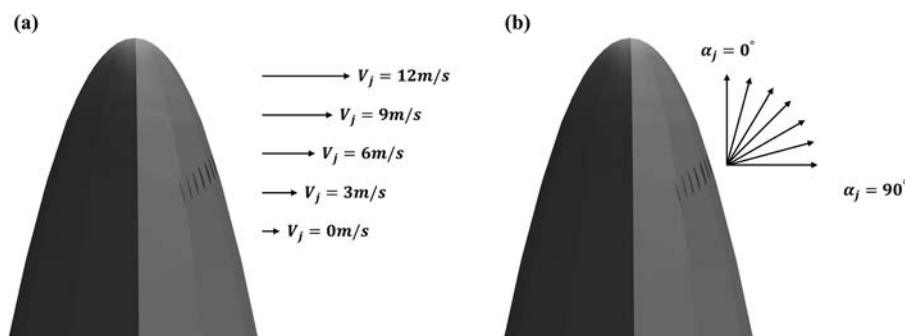


FIG. 14. Parametric control of water injection under different (a) injection velocities and (b) injection angles.

TABLE V. Time-averaged coefficients under the different injection velocities.

Positions of holes	V_J (m/s)	C_l	C_d
S/I	0	0.547	0.0388
S/I	3	0.547	0.0388
S/I	6	0.546	0.0387
S/I	9	0.545	0.0387
S/I	12	0.545	0.0387

control of water injection. Because the side injection method could better inhibit TVC, this condition was used during parametric control.

First, the injection velocity was varied during TVC control, where from 0 to 12 m/s, the injection velocity, V_J , could be divided into five grades. Subsequently, the influence of this parameter on TVC suppression was analyzed [Fig. 14(a)].

Table V lists the lift and drag coefficients along with the different injection velocities used to determine the influence of injection velocity on the hydrodynamic performance of the hydrofoil. Similar to the results presented in Subsection V A, as the velocity of the injecting water increased, the hydrodynamic performance was almost the same. This meant that after injection from the holes, the injecting fluid was only concentrated in the ambient region of the tip vortex and would not significantly impact the flow around the hydrofoil.

In the next step, the TVC structures and time-averaged cavity volumes under the different injection velocities were illustrated, as shown in Figs. 15 and 16, respectively.

Figure 15(a) shows that when S/I was not involved, the TVC structure consisted of a slender bubble and could develop for a long distance downstream.

Second, under $V_J = 3$ m/s, as shown in Fig. 15(b), the diameter and development length of the TVC decreased compared to the structure shown in Fig. 15(a), where one discontinuous point occurred in the middle of the TVC. Moreover, when the injection velocity increased to 9 m/s, TVC almost disappeared and its structure became illegible.

Third, a comparison of Figs. 15(a)–15(d) revealed that as the injection velocity increased, the first position of discontinuous points of TVC (marked by the black arrows) moved forward. Hence, as the injection velocity increased, the degree of cavitation instability also increased. Furthermore, the effect of injection velocity was limited. According to the results shown in Figs. 15(d) and 15(e), when the injection velocity was increased to 12 m/s, the structure of TVC was similar to that in Fig. 15(d).

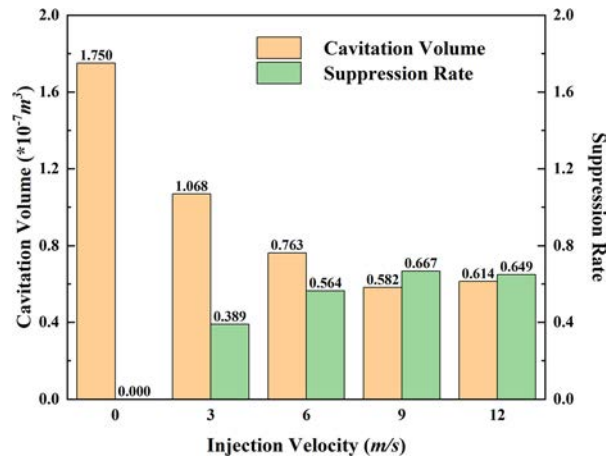


FIG. 16. Time-averaged cavity volumes and suppression rates under different injection velocities.

The time-averaged cavity volumes under the five injection velocities are depicted in Fig. 16, as the TVC structure shown in Fig. 15 was instantaneous and the results obtained by analyzing this structure were possibly accidental. As shown in Fig. 16, each injection velocity could effectively suppress TVC. When the injection velocity was less than 9 m/s, the TVC suppression rates increased as the injection velocity increased, whereas the gradients of the suppression rate decreased at the same time. However, when $V_J = 12$ m/s, the time-averaged cavity volume was $0.614 \times 10^{-7} m^3$ and was slightly higher than the volume at $V_J = 9$ m/s. The results showed that increasing the injection velocity could increase TVC inhibition, but when the velocity reached a certain value (9 m/s in this study), the inhibition effect would no longer increase. Furthermore, because the velocity was only divided into five grades, the optimal injection velocity for TVC suppression could not be accurately determined.

To further clarify the influence of injection velocity on the tip vortex, the instantaneous vorticity fields at $x = 0-1 C$ were illustrated, as shown in Fig. 17. As presented in Fig. 17(a), without water injection, the tip vortex first increased at $x = 0 C$. At this position, the vortex had the strongest rotating strength, but the smallest diameter. When the tip vortex was developed to the position of $x = 0.1 C$, its diameter was enlarged by TVC. Subsequently, the tip vortex matured to form a complete circle at $x = 0.4 C$. Comparing the contours from upstream to downstream in Fig. 17(a) clearly showed that after the tip vortex

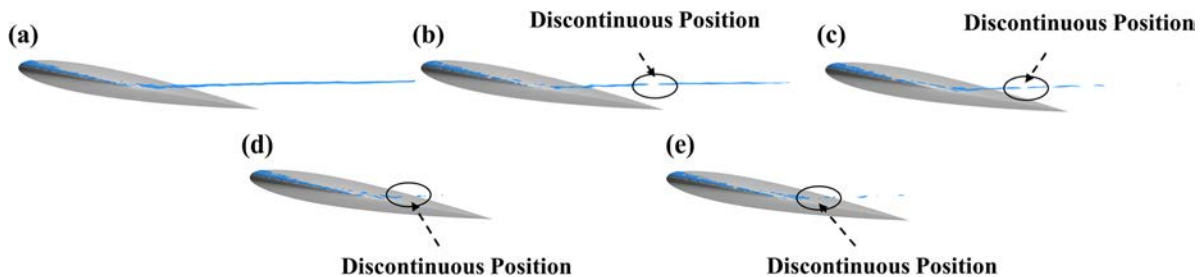


FIG. 15. TVC structures under different injection velocities: (a) $V_J = 0$, (b) $V_J = 3$, (c) $V_J = 6$, (d) $V_J = 9$, and (e) $V_J = 12$ m/s.

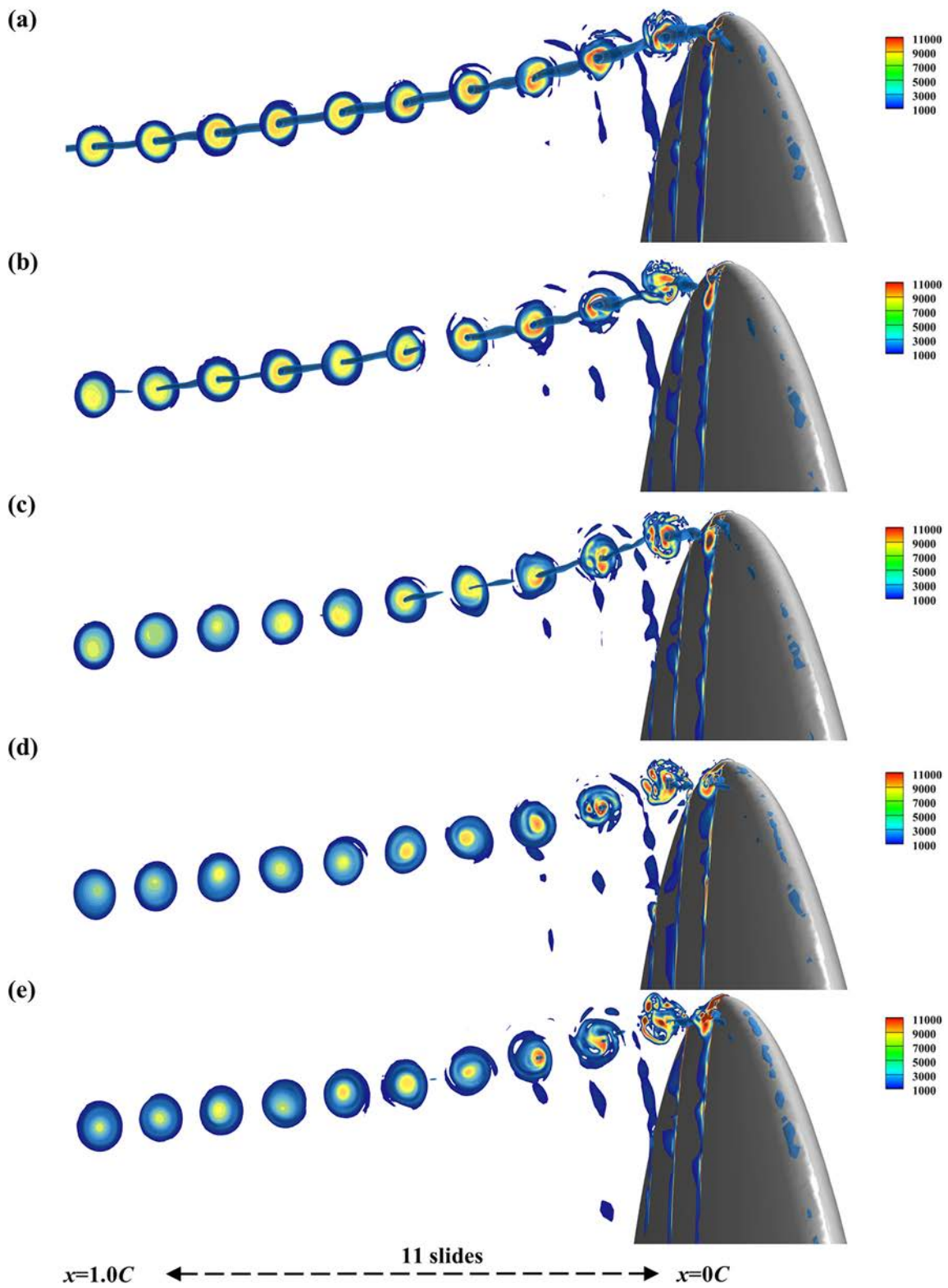


FIG. 17. Contours of $|\omega_x|$ comparison for different injection velocities: (a) $V_j = 0$, (b) $V_j = 3$, (c) $V_j = 6$, (d) $V_j = 9$, and (e) $V_j = 12$ m/s.

completely formed, its structure was unchanged, but its rotating strength gradually decreased.

When water was injected into the tip vortex region, the development of the tip vortex changed. Initially, at the TVC inception position, the tip vortex structure was dramatically deformed. Then, when the deformed vortices developed toward the downstream ($x = 0.2 C$ to $x = 0.4 C$ in Fig. 17), they merged with each other and reformed into one vortex. Finally, the reformed tip vortex continued to develop backward and gradually dissipated. Therefore, if water injection was not included in the calculations, the tip vortex underwent only three stages of development, namely, inception, growth, and dissipation. However, with side injection, the tip vortex deformed at the inception stage, and the growth stage was accompanied by the merging stage. As the injection velocity increased, the deformation of the tip vortex increased and the degree of decrease in vorticity intensity during the merging process increased.

Furthermore, from $x = 0-1 C$, the surface-averaged intensities of the vortices, $\bar{\omega}$, were visualized, as shown in Fig. 18. The curves in Fig. 18 showed the trends of $\bar{\omega}$ from the upstream to the downstream under the different injection velocities, where the histograms in the figure indicated the sums of the vorticity intensities in the tip vortex cores under the five conditions. For isolating the vortex core region, only the areas with $|\omega_x|$ above 5000 were used in the calculation. The definition of $\bar{\omega}$ was as follows:

$$\bar{\omega} = \frac{\iint \omega_{core} dydz}{\iint S_{core} dydz}, \tag{19}$$

where ω_{core} is the $|\omega_x|$ value in the vortex core region, S_{core} is the area of the vortex core region, and $|\omega_x|$ is the redefinition of vorticity distribution along the streamwise direction. By taking only the absolute value, $|\omega_x|$ ignored the rotation direction of the vortex and only extracted its intensity. Therefore, ω_{core} redefined the distribution of $|\omega_x|$. We only recorded the distribution of $|\omega_x|$ when its value was higher than 5000. Based on this process, the sum of vorticity intensities at the tip vortex core on each surface [the molecules in Eq. (18) denoted as ω_{total}] could be easily calculated. S_{core} only identified those

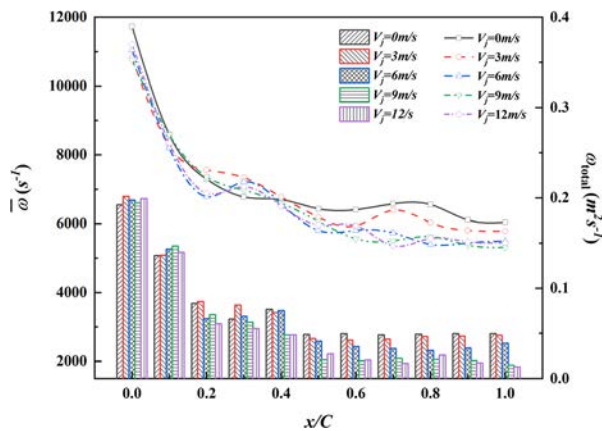


FIG. 18. Variation in the averaged vorticity strengths under different injection velocities.

positions whose $|\omega_x|$ value was above 5000, and after surface integration, the total area of the vortex core on each surface [the denominator in Eq. (18) denoted as S_{total}] could be obtained.

As shown in Fig. 18, when focusing on the distribution of ω_{total} , before $x = 0-1 C$, ω_{total} indicated that the vortex tended to diffuse from upstream to downstream. Furthermore, the values of ω_{total} only showed slight differences under the five conditions. From $x = 0.1 C$ to $x = 0.3 C$, in the forming stage of the tip vortex, the shape of the tip vortex gradually became circular, but the strength was considerably reduced. Then, from $x = 0.5 C$ to $x = 1.0 C$, the total intensities of the tip vortices gradually stabilized. At this stage, ω_{total} gradually decreased with an increase in the injection velocity.

The changes in the $\bar{\omega}$ distribution along with x/C were similar to ω_{total} . However, from $x = 0.3 C$ to $x = 0.4 C$, the distributions of $\bar{\omega}$ under water injection showed an obvious downward trend, which was not found under $V_j = 0$ m/s. As shown in Fig. 17, this process was called the merging stage. After merging, $\bar{\omega}$ distributions within water injection decreased to a level lower compared to under no injection. In addition, when the tip vortex was developed to $x = 1.0 C$, the distributions of $\bar{\omega}$ under all injection velocity conditions showed trends analogous to the distributions of the cavity volume.

According to Figs. 17 and 18, the energy carried by the injecting water caused vortex structure deformation at the inception position of the tip vortex, which reduced the strength of the tip vortex. At the same time, similar to cavitation suppression, when V_j was less than 9 m/s, an increase in injection velocity would continuously increase the degree of reduction in the rotation intensity of the tip vortex.

C. Injecting angle control in the water injection methods

Next, the injection angle, α_j , had been changed to identify its effects on TVC control [Fig. 14(b)]. Similar to the injection velocity, from injection along the z direction to injection along the y direction, α_j was divided into seven grades and the changes in the hydrodynamic parameters, cavitation bubbles, and the tip vortex structures along with different α_j are given below. When the injection angles were variable, the velocity was constant and $V_j = 9$ m/s.

First, the hydrodynamic performance of the hydrofoil at different injection angles was compared, as given in Table VI. Upon varying the injection angles, the maximum differences among the C_l and C_d values were 0.002 and 0.0002, respectively, which were negligible during

TABLE VI. Time-averaged coefficients under different injection angles.

Positions of the holes	α_j	C_l	C_d
S/I	W/O	0.547	0.0388
S/I	0	0.547	0.0387
S/I	15	0.546	0.0386
S/I	30	0.546	0.0388
S/I	45	0.545	0.0387
S/I	60	0.545	0.0388
S/I	75	0.545	0.0387
S/I	90	0.545	0.0387

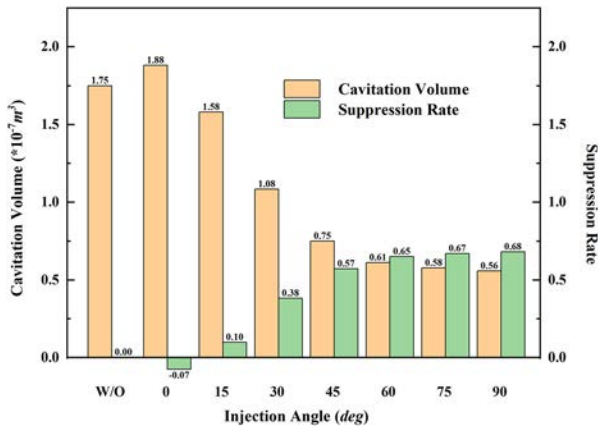


FIG. 19. Time-averaged cavity volumes and suppression rates under different injection angles.

working. Therefore, the hydrodynamic performance (lift and drag coefficients) of the elliptical hydrofoil had a negligible relationship with changes in α_j , which was similar to that under different injection velocities.

Second, the time-averaged cavity volume and its suppression rate are illustrated in Fig. 19, and the TVC structures under the eight injection angles are shown in Fig. 20. It was evident that as the injection angle increased, the suppression effect of water injection on TVC generation increased. However, the gradient of the suppression rate was reduced.

Furthermore, as shown in Fig. 19, when water was injected along the z direction, the time-averaged cavity volume was $1.88 \times 10^{-7} \text{ m}^3$ and its suppression rate was -7% . This meant that when the injection holes were located on the suction surface of the hydrofoil, directional injection favored the generation of TVC instead of inhibiting it. By contrast, the y -directional injection ($\alpha_j = 90^\circ$) could effectively decrease the cavity volume, and the suppression rate under this condition could be as high as 68%.

As shown in Fig. 20, when the injection angle was less than 45° , almost no discontinuous points were observed in the cavitation bubbles during the development of TVC. A discontinuous point first appeared in Fig. 20(e), in which the injected water could directly act on the cavitation structures and subsequently increase the instability

of the flow. Hence, the presence of discontinuity meant that flow in the region was unstable. The phenomenon shown in Fig. 15(b) also verified this conclusion, where the injected water could directly act on the TVC; thus, even if the velocity was extremely low, the discontinuity was still found in the middle of the TVC.

Third, as shown in Fig. 21, the influences of different injection angles on vorticity development were visualized, which were concretely determined by the destruction of the tip vortex structure at the inception position ($x = 0.1 C$ position) and the corresponding weakening of the tip vortex core at the downstream region.

The agitation degree of injection flow to the inception tip vortex increased from $\alpha_j = 0^\circ$ to $\alpha_j = 90^\circ$. Under $\alpha_j = 0^\circ$, the shape of the tip vortex was similar to that obtained without injection. When the injection angle increased to 15° and 30° , the vortex structure deformed at $x = 0.1 C$ and returned to normal in the next sliding position. From deformation to normalization, the recovery process corresponded to 0.1, as shown in Figs. 21(b) and 21(c). Moreover, as shown in Figs. 21(d)–21(h), the recovery process from deformation to normal was extended.

However, the suppression rate of the strength of tip vortex flow increased as the injection angle increased. As shown in Fig. 21, the diameter of the tip vortex (yellow region) and the final position of the vortex core were effective parameters for evaluating the vortex strength of the flow. As shown in Figs. 21(a)–21(c), the suppression effect of water injection was rather small, TVC moved to the downstream region, and the tip vortices were very similar. Figures 21(c)–21(f) show that the diameter of the tip vortex core tended to gradually shrink, and Figs. 21(f)–21(h) show that the diameter of the vortex core no longer decreased, while the final position of the vortex core continued to move forward.

VI. SUMMARY

In this study, based on the LES turbulence model and Schnerr-Sauer cavitation model, the TVC of an NACA0012 elliptical hydrofoil was numerically analyzed. First, the wetted and cavitating conditions were simulated to analyze the mechanism of tip vortex generation and its cavitation. Then, two injection methods, namely, side and top injection (S/I and T/I, respectively), were used to control TVC, and the results showed that water injection could effectively suppress the TVC development. Finally, the injection velocities and angles under S/I were varied to determine their impact on the tip vortex formation and TVC.

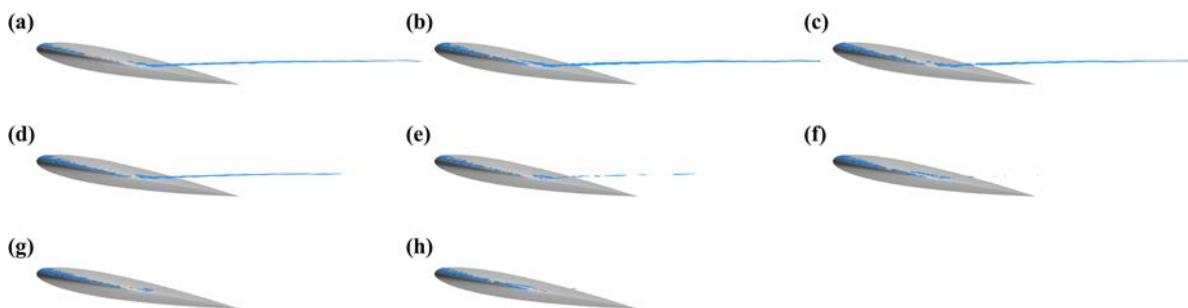


FIG. 20. TVC structures under different injection angles: (a) without injection, (b) $\alpha_j = 0^\circ$, (c) $\alpha_j = 15^\circ$, (d) $\alpha_j = 30^\circ$, (e) $\alpha_j = 45^\circ$, (f) $\alpha_j = 60^\circ$, (g) $\alpha_j = 75^\circ$, and (h) $\alpha_j = 90^\circ$.

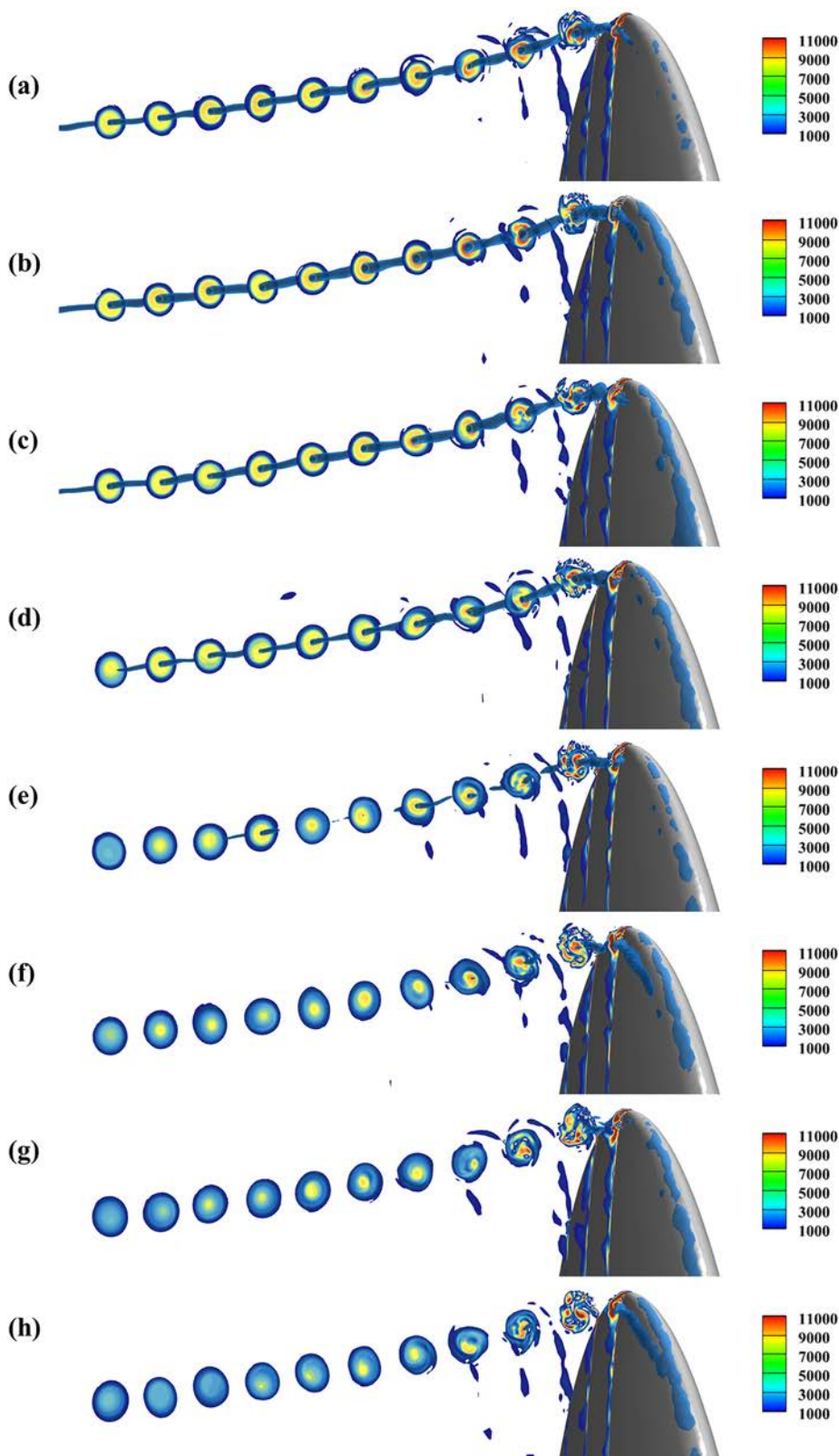


FIG. 21. Contours of $|\omega_x|$ at different injection angles: (a) W/O, (b) $\alpha_j = 0^\circ$, (c) $\alpha_j = 15^\circ$, (d) $\alpha_j = 30^\circ$, (e) $\alpha_j = 45^\circ$, (f) $\alpha_j = 60^\circ$, (g) $\alpha_j = 75^\circ$, and (h) $\alpha_j = 90^\circ$.

1. The generation of TVC was related to the swirling effect of the tip vortex. After TVC occurred, it decreased the strength of the vortex in the core region and reshaped its structure.
2. Both the T/I and S/I methods could effectively inhibit the generation of TVC, but they only had a slight impact on the hydrodynamic performance of the hydrofoil. T/I could only change the magnitude and direction of the vortex rotating flow, and side injection could directly break the formation of the tip vortex. Therefore, S/I was more effective in controlling TVC than T/I.
3. Under S/I, a certain increase in the injection velocity could dramatically enhance TVC inhibition. The maximum effective injection velocity in this study was 9 m/s. Moreover, increasing the injection angle could effectively control TVC. In addition, the impact of injection flow on vortex deformation mainly occurred around the injection holes. Then, the deformed vortices would merge with each other and recover to their circular shape in the downstream region. Increasing the injection velocity or angle could extend the recovery process.
4. Future studies will focus on optimizing water injection and determining the optimal location of the injection holes.

ACKNOWLEDGMENTS

This work is supported by the National Natural Science Foundation of China, Grant Nos. 52001210 and 52131102, for which the authors are most grateful.

AUTHOR DECLARATIONS

Conflict of interest

The authors have no conflicts to disclose.

Author Contributions

Kang Liu: Conceptualization (equal); formal analysis (equal); investigation (equal); methodology (equal); validation (equal); visualization (equal) and original draft preparation (lead). **Ping Wei:** investigation (equal); project administration (equal) and validation (equal). **Liushuai Cao:** conceptualization (equal); data curation (equal); funding acquisition (lead); investigation (equal); methodology (equal) and project administration (equal). **Decheng Wan:** funding acquisition (lead); resources (lead) and supervision (lead).

DATA AVAILABILITY

The data that support the findings of this study are available from the corresponding author upon reasonable request.

REFERENCES

- ¹K. Kindler, E. Goldhahn, F. Leopold, and M. Raffel, "Recent developments in background oriented schlieren methods for rotor blade tip vortex measurements," *Exp. Fluids* **43**, 233 (2007).
- ²R. Mailach, I. Lehmann, and K. Vogeler, "Rotating instabilities in an axial compressor originating from the fluctuating blade tip vortex," *J. Turbomach.* **123**, 453 (2001).
- ³G. Batchelor, "Axial flow in trailing line vortices," *J. Fluid Mech.* **20**, 645 (1964).
- ⁴R. Arndt, V. Arakeri, and H. Higuchi, "Some observations of tip-vortex cavitation," *J. Fluid Mech.* **229**, 269 (1991).
- ⁵O. Boulon, J.-P. Franc, and J.-M. Michel, "Tip vortex cavitation on an oscillating hydrofoil," *J. Fluids Eng.* **119**, 752 (1997).
- ⁶J.-K. Choi and G. L. Chahine, "Noise due to extreme bubble deformation near inception of tip vortex cavitation," *Phys. Fluids* **16**, 2411 (2004).
- ⁷C.-T. Hsiao and G. L. Chahine, "Effect of vortex/vortex interaction on bubble dynamics and cavitation noise," in Fifth International Symposium on Cavitation (CAV2003), 2003.
- ⁸B. Ji, X. Luo, R. E. Arndt, and Y. Wu, "Numerical simulation of three dimensional cavitation shedding dynamics with special emphasis on cavitation-vortex interaction," *Ocean Eng.* **87**, 64 (2014).
- ⁹H. Cheng, X. Bai, X. Long, B. Ji, X. Peng, and M. Farhat, "Large eddy simulation of the tip-leakage cavitating flow with an insight on how cavitation influences vorticity and turbulence," *Appl. Math. Modell.* **77**, 788 (2020).
- ¹⁰C. Xie, J. Liu, J.-W. Jiang, and W.-X. Huang, "Numerical study on wetted and cavitating tip-vortical flows around an elliptical hydrofoil: Interplay of cavitation, vortices, and turbulence," *Phys. Fluids* **33**, 093316 (2021).
- ¹¹T. Ohta and R. Sugiura, "Numerical prediction of interaction between turbulence structures and vortex cavitation," *J. Turbul.* **20**, 599 (2019).
- ¹²E. Kadivar, O. el Moctar, and K. Javadi, "Investigation of the effect of cavitation passive control on the dynamics of unsteady cloud cavitation," *Appl. Math. Modell.* **64**, 333 (2018).
- ¹³E. Kadivar, M. V. Timoshevskiy, K. S. Pervunin, and O. E. Moctar, "Experimental and numerical study of the cavitation surge passive control around a semi-circular leading-edge flat plate," *J. Mar. Sci. Technol.* **25**, 1010 (2020).
- ¹⁴G. Zhao, L. Cao, B. Che, R. Wu, S. Yang, and D. Wu, "Towards the control of blade cavitation in a waterjet pump with inlet guide vanes: Passive control by obstacles," *Ocean Eng.* **231**, 108820 (2021).
- ¹⁵U. Svennberg, A. Asnaghi, R. Gustafsson, and R. E. Bensow, "Experimental analysis of tip vortex cavitation mitigation by controlled surface roughness," *J. Hydrodyn.* **32**, 1059 (2020).
- ¹⁶A. Asnaghi, U. Svennberg, R. Gustafsson, and R. E. Bensow, "Propeller tip vortex mitigation by roughness application," *Appl. Ocean Res.* **106**, 102449 (2021).
- ¹⁷A. Amini, J. Seo, S. H. Rhee, and M. Farhat, "Mitigating tip vortex cavitation by a flexible trailing thread," *Phys. Fluids* **31**, 127103 (2019).
- ¹⁸M. Zaresharif, F. Ravelet, D. J. Kinahan, and Y. M. Delaure, "Cavitation control using passive flow control techniques," *Phys. Fluids* **33**, 121301 (2021).
- ¹⁹T. Capurso, G. Menchise, G. Caramia, S. Camporeale, B. Fortunato, and M. Torresi, "Investigation of a passive control system for limiting cavitation inside turbomachinery under different operating conditions," *Energy Procedia* **148**, 416 (2018).
- ²⁰M.-R. Erfanian and M. Moghiman, "Experimental investigation of critical air entrainment in ventilated cavitating flow for a forward facing model," *Appl. Ocean Res.* **97**, 102089 (2020).
- ²¹G. Chahine, G. Frederick, and R. Bateman, "Propeller tip vortex cavitation suppression using selective polymer injection," *Fluids Eng.* **115** (1993).
- ²²W. Wang, T. Tang, Q. Zhang, X. Wang, Z. An, T. Tong, and Z. Li, "Effect of water injection on the cavitation control: Experiments on a NACA66 (MOD) hydrofoil," *Acta Mech. Sin.* **36**, 999 (2020).
- ²³M. V. Timoshevskiy and I. I. Zapryagaev, "Generation of a wall jet to control unsteady cavitation over a 2D hydrofoil: Visualization and hydroacoustic signal analysis," *J. Phys.: Conf. Ser.* **899**, 032021 (2017).
- ²⁴S.-L. Park, S.-J. Lee, G.-S. You, and J.-C. Suh, "An experimental study on tip vortex cavitation suppression in a marine propeller," *J. Ship Res.* **58**, 157 (2014).
- ²⁵S. Lu, W. Wang, and X. Wang, "Experiment research on cavitation control by active injection," in The 10th International Symposium on Cavitation, 2018.
- ²⁶C.-S. Lee, B.-K. Ahn, J.-M. Han, and J.-H. Kim, "Propeller tip vortex cavitation control and induced noise suppression by water injection," *J. Mar. Sci. Technol.* **23**, 453 (2018).
- ²⁷W. Zhao and G. Zhao, "An active method to control cavitation in a centrifugal pump by obstacles," *Adv. Mech. Eng.* **9**, 168781401773294 (2017).
- ²⁸M. G. De Giorgi, A. Ficarella, and D. Fontanarosa, "Active Control of Unsteady Cavitating Flows in Turbomachinery," in Proceedings of the ASME Turbo Expo 2019: Turbomachinery Technical Conference and Exposition, 2019.

- ²⁹W. Wang, Q. Zhang, T. Tang, S. Lu, Q. Yi, and X. Wang, "Numerical study of the impact of water injection holes arrangement on cavitation flow control," *Sci. Prog.* **103**, 1 (2020).
- ³⁰W. Wang, Z. Li, M. Liu, and X. Ji, "Influence of water injection on broadband noise and hydrodynamic performance for a NACA66 (MOD) hydrofoil under cloud cavitating condition," *Appl. Ocean Res.* **115**, 102858 (2021).
- ³¹C. S. Pant and S. H. Frankel, "Interaction between surface blowing and re-entrant jet in active control of hydrofoil cavitation," *Ocean Eng.* **242**, 110087 (2021).
- ³²X. Zhang, Z. Liu, L. Cao, and D. Wan, "Tip clearance effect on the tip leakage vortex evolution and wake instability of a ducted propeller," *JMSE* **10**, 1007 (2022).
- ³³A. Asnaghi, R. E. Bensow, and U. Svnennberg, *Comparative Analysis of Tip Vortex Flow Using RANS and LES* (CIMNE, 2017).
- ³⁴M. Ge, U. Svnennberg, and R. E. Bensow, "Investigation on RANS prediction of propeller induced pressure pulses and sheet-tip cavitation interactions in behind Hull condition," *Ocean Eng.* **209**, 107503 (2020).
- ³⁵J. Decaix, G. Balarac, M. Dreyer, M. Farhat, and C. Münch, "RANS and LES computations of the tip-leakage vortex for different gap widths," *J. Turbul.* **16**, 309 (2015).
- ³⁶N. Yilmaz, M. Atlar, and M. Khorasanchi, "An improved Mesh Adaption and Refinement approach to Cavitation Simulation (MARCS) of propellers," *Ocean Eng.* **171**, 139 (2019).
- ³⁷J. Hu, W. Zhang, C. Wang, S. Sun, and C. Guo, "Impact of skew on propeller tip vortex cavitation," *Ocean Eng.* **220**, 108479 (2021).
- ³⁸N. Yilmaz, B. Aktas, M. Atlar, P. A. Fitzsimmons, and M. Felli, "An experimental and numerical investigation of Propeller-Rudder-Hull interaction in the presence of tip vortex cavitation (TVC)," *Ocean Eng.* **216**, 108024 (2020).
- ³⁹Y. Long, X. Long, B. Ji, and T. Xing, "Verification and validation of Large Eddy Simulation of attached cavitating flow around a Clark-Y hydrofoil," *Int. J. Multiphase Flow* **115**, 93 (2019).
- ⁴⁰Simcenter STAR-CCM+ User Guide (2020).
- ⁴¹M. Nezamirad, A. Yazdi, S. Amirahmadian, N. Sabetpour, and A. Hamed, "Utilization of Schnerr-Sauer cavitation model for simulation of cavitation inception and super cavitation," *Int. J. Aerosp. Mech. Eng.* **16**, 36 (2022), see https://www.researchgate.net/publication/359013772_Utilization_of_Schnerr-Sauer_Cavitation_Model_for_Simulation_of_Cavitation_Inception_and_Super-Cavitation.
- ⁴²D.-Q. Li, M. Grekula, and P. Lindell, "A modified SST $k-\omega$ turbulence model to predict the steady and unsteady sheet cavitation on 2D and 3D hydrofoils," in 7th International Symposium on Cavitation, 2009.
- ⁴³V. Lomakin and O. Bibik, "Numerical prediction of the gas content effect on the cavitation characteristics of the pump using the simplified Rayleigh-Plesset equation," *IOP Conf. Ser.* **492**, 012037 (2019).
- ⁴⁴M-s Zhao, W-w Zhao, and D-c Wan, "Numerical simulations of propeller cavitation flows based on OpenFOAM," *J. Hydrodyn.* **32**, 1071 (2020).
- ⁴⁵J. Sauer and G. Schnerr, "Development of a new cavitation model based on bubble dynamics," *Z. Angew. Math. Mech.* **81**, 561 (2001).
- ⁴⁶N. Takasugi, H. Yamaguchi, H. Kato, and M. Maeda, "An experiment of cavitating flow around a finite span hydrofoil," *J. Soc. Nav. Archit. Japan* **1992**, 257.
- ⁴⁷N. N. Ahmad, F. H. Proctor, and R. B. Perry, "Numerical simulation of the aircraft wake vortex flowfield," in 5th AIAA Atmospheric and Space Environments Conference, 2013.
- ⁴⁸A. Asnaghi, U. Svnennberg, and R. E. Bensow, "Large eddy simulations of cavitating tip vortex flows," *Ocean Eng.* **195**, 106703 (2020).
- ⁴⁹N. Garg, B. W. Pearce, P. A. Brandner, A. W. Phillips, J. R. Martins, and Y. L. Young, "Experimental investigation of a hydrofoil designed via hydrostructural optimization," *J. Fluids Struct.* **84**, 243 (2019).
- ⁵⁰Z. Ni, M. Dhanak, and T.-C. Su, "Performance of a slotted hydrofoil operating close to a free surface over a range of angles of attack," *Ocean Eng.* **188**, 106296 (2019).
- ⁵¹Y. Liu and L. Tan, "Method of C groove on vortex suppression and energy performance improvement for a NACA0009 hydrofoil with tip clearance in tidal energy," *Energy* **155**, 448 (2018).